

Sintering and Crystallization of Fluoride-Containing Bioactive Glass F3

Carsten Blaeß^{1,*} , Aldo R. Boccaccini² , and Ralf Müller^{1,3}

¹Bundesanstalt für Materialforschung und -prüfung (BAM), Richard-Willstätter-Straße 11, 12489 Berlin, Germany

²Friedrich-Alexander University Erlangen-Nuremberg, Institute of Biomaterials, Ulrich-Schalk-Straße 3, 910506 Erlangen, Germany

³Clausthal University of Technology, Institute of Non-Metallic Materials, Zehntnerstraße 2a, 38678 Clausthal-Zellerfeld, Germany

*Corresponding author: Carsten Blaeß, carsten.blaess@bam.de

Abstract. The fluoride-containing bioactive glass F3 with nominal composition (mol%) 44.8 SiO₂ - 2.5 P₂O₃ - 36.5 CaO - 6.6 Na₂O - 6.6 K₂O - 3.0 CaF₂ is a highly promising candidate for bone replacement applications. Its strong crystallization tendency, however, requires a thorough understanding of the interplay between glass powder particle size, surface crystallization, and sintering. Therefore, this study characterizes the sintering and crystallization of bulk specimens and various particle size fractions by differential thermal-analysis, laser scanning, electron microscopy, X-ray diffraction, and Infrared spectroscopy. Particle size fractions < 56 µm were found to fully densify, while crystals growing from the glass particle surface retard sintering of coarser fractions. Small amounts of a non-stoichiometrically calcium phosphosilicate (Ca_{14.92}(PO₄)_{2.35}(SiO₄)_{5.65}) occurs as the primary crystal phase followed by combeite (Na₄Ca₄[Si₆O₁₈]) as a temporarily dominating phase. The surface crystallization of both phases was found to be mainly responsible for sinter retardation. During later stages of crystallization, additional phases such as cuspidine (Ca₄F₂Si₂O₇) and silicorhenanite (Na₂Ca₄(PO₄)₂SiO₄) occur, but finally monoclinic wollastonite (CaSiO₃) forms as the dominant phase.

Keywords: Bioactive Glass, Sintering, Crystallization

1. Introduction

Fluoride-containing bioactive glasses (BG) are highly promising candidate materials for dental remineralization and artificial bone replacement [1]. They release fluoride ions during dissolution [2], [3], [4], [5] which reduces tooth demineralization [6] due to the formation of fluorapatite (FAp) [7], [2]. FAp has a higher mechanical strength [8], [9] and is more resistant to acid attack than hydroxyapatite (HAp) [10], [11]. Further, the incorporation of fluoride into human bone structure increases its density which is of interest for the prevention of fractures and osteoporosis [12], [13].

One interesting glass in this group is the BG “F3” with the nominal composition (mol%) 44.8 SiO₂ - 2.5 P₂O₃ - 36.5 CaO - 6.6 Na₂O - 6.6 K₂O - 3.0 CaF₂ [14], [15]. BG F3 shows an ion release behavior similar to that of the well-known Bioglass® 45S5 [16] in TRIS buffer solution [14]. BG F3 is similarly biocompatible and supports the proliferation and attachment of pre-osteoblast cells (MC3T3-E1) [17]. In contrast to the well-known Bioglass® 45S5, however, BG F3 provides much better processability, allowing, for instance, fiber drawing [18] and sintering of dense glassy compacts [15], [19], whereas sintering of BG 45S5 powders is strongly affected by the crystallization of combeite (Na₂CaSi₂O₆ or Na₂Ca₂Si₃O₉) [20], [21], [22]. On the other

hand, sinter retardation of BG F3 powders, caused by concomitant surface crystallization, depends on glass particle size [15]. In this way, surface-induced crystallization could be a wishful tool to tune the degree of densification by varying the particle size [15]. This additional degree of freedom in the manufacture of sintered BG compacts would be highly beneficial to tailor the microporosity and surface roughness of sintered powder compacts. For the manufacture of complex-shaped bone replacement implants and scaffolds using additive manufacturing [23], [24], this possibility could yield remarkable benefits but also could cause major problems.

Against this background, this study was carried out to contribute to a better understanding of the surface-induced crystallization of BG F3. This includes the crystallization sequence, the sinter retardation effect of the primary phases, and the effect of glass particle size and fluoride content on the complex sintering-crystallization interplay.

2. Experimental

2.1 Samples

BG F3 was prepared from reagent grade SiO₂ (Quarzweke Frechen, Frechen, Germany), CaCO₃, Na₂CO₃, K₂CO₃ (Merck, Darmstadt, Germany), NaPO₃ and CaF₂ (Karl Roth, Karlsruhe, Germany) raw materials. A batch of 4500 g was molten in a 2-liter Pt crucible at 1250 °C and refined for 1 hour at 1350 °C using a medium frequency inductive furnace (EMA-TEC, Sonderhausen, Germany). A glass frit and a glass block were produced by casting the glass melt into water and onto a steel mold, respectively. The latter was placed into a muffle furnace and cooled from 600 °C to room temperature overnight. Glass powders were produced by crushing the vacuum-dried glass frit using zirconia jaws (BB51, Retsch, Haan, Germany). This powder was then sieved to twelve particle size fractions (psf) in the range of <32 µm to 315 µm (Table S1 in the supplementary material¹).

2.2 Methods

Glass composition was measured on bulk samples of 28×28×28 mm³ with an XRF Zetium Ultimate Analyzer (Malvern Panalytical B.V., Almelo, Netherlands) using 4-kW Rh radiation and a 20 min exposure. The fluoride content was double-checked by pyrohydrolysis applying the standard procedure of DIN 51084:2008-11 by treating the powdered glass in an atmosphere saturated with water vapor at approximately 1000 °C and measuring the extracted fluoride in the watery solution using a fluorosensitive electrode. The glass density, ρ , was measured by Archimedes' method in deionized water at 21.5 °C and 98.95 kPa (742.2 mmHg).

The coefficient of thermal expansion, α_{300} , and the dilatometric softening point, T_{s-Dil} , were determined on glass beams of 25×5×5 mm³ by dilatometry (DIL402c, Netzsch, Selb, Germany) at 5 K/min between 20 and 300 °C with ±2 K accuracy.

Glass transition temperature, T_{g-DTA} , and overall crystallization kinetics were studied on 12-16 mg samples in Pt crucibles at 10 K/min using a thermobalance TAG24 (Setaram, Caluire, France) within 5 K accuracy and Al₂O₃ as reference material. Measurements were performed in dry synthetic air (oxygen/nitrogen = 20/80) and argon at 45 mL/min.

For crystallization and sintering heat treatments, a heating microscope (Leitz, Wetzlar, Germany) was used with 7 K temperature accuracy. To prevent thermal shock, cracking, and spalling after annealing, the samples were cooled within this furnace at 41 K/min to 400 °C

¹ Supplementary material is available at: <https://doi.org/10.5281/zenodo.15261386>

before cooling freely due to the furnace's thermal capacity. The cooling regime was found to have no significant influence on crystallization and sintering.

The relative powder compact density, ρ_{rel} , during sintering, was studied on cylindrical powder compacts of 5 mm in diameter and height, uniaxial pressed at 50 MPa for 30 s and heated at 10 K/min on zirconia substrates (Ceramtec, Plochingen, Germany).

Crystal phases were detected on powder compacts heated to certain temperatures at 10 K/min before being cooled in the heating microscope furnace as described above. Afterward, samples were crushed in a steel mortar. One part of the crushed compacts was then sputter-coated with carbon and analyzed in an environmental electron microscope (ESEM, XL-30, Philips, Hamburg, Germany) equipped with a tungsten cathode at 20 kV (FEI, Eindhoven, Netherlands, electronics upgraded by point electronic GmbH in 2020). An Energy-Dispersive X-ray system (EDX, Quantax 200, Bruker Nano GmbH, X Flash 6/60 SDD) was used for chemical analysis. Both ESEM and EDX investigations were performed in the "high-vacuum mode" of the microscope. The signal was measured with a Back Scatter Electron detector (BSE). The corresponding EDX spectra were collected at an accelerating voltage of 15 keV and the quantification was performed standardless.

The other part of the crushed compacts was milled in a vibratory ball mill (PULVERISETTE 23, Fritsch, Idar-Oberstein, Germany) for 30 s at 45 s^{-1} in a zirconia jar bearing two $\varnothing 10 \text{ mm}$ zirconia balls. Immediately after milling, these powders were studied with attenuated total reflection Fourier transformed infrared spectroscopy, ATR-FTIR, using a Nicolet iN10 Analyzer (Thermo Fischer Scientific, Waltham, Massachusetts, USA) equipped with Ga crystal and MCT-A detector. Further, qualitative X-ray diffraction measurements (XRD), were performed between 5 and $80^\circ 2\theta$ in steps of 0.02° each 60 min using Cu $K\alpha$ radiation and a Lynxeye detector on a D8 Discover diffractometer (Bruker AXS, Karlsruhe, Germany). For phase analysis of the diffraction pattern, the software tool "Match!" was used (Dr. H. Putz & Dr. K. Brandenburg GbR, Bonn, Germany).

Surface crystal diameter, D , the thickness of the crystalline surface layer, L , and the surface nucleation density, N_s , were investigated on sawed $5 \times 5 \times 5 \text{ mm}^3$ glass cubes heated at 10 K/min to different temperatures, T_x (non-isothermal treatment), or heated at 30 K/min to $T_x - 10 \text{ K}$ and 5 K/min to T_x before being hold at this temperature for up to 80 min (isothermal treatment). Heat-treated cubes were ground from the top surface water-free on SiC-grinding discs (1200 and 2000 grade) and polished with $3 \mu\text{m}$ diamond suspension (Struers, Willich, Germany). Such treated samples were then studied with a confocal laser scanning microscope (LEXT OLS 4100, Olympus, Tokyo, Japan) using 400-420 nm laser light.

3. Results

3.1 Glass properties

Table 1 compares the targeted (nominal) and measured chemical composition of BG F3. The measured glass composition matches well the target values although a minor increase in Na_2O and K_2O of 0.4 mol% is evident. Table 2 lists other glass properties.

Table 1. Glass composition in mol%.

	SiO_2	P_2O_5	CaO	Na_2O	K_2O	CaF_2
Nominal	44.8	2.5	36.5	6.6	6.6	3.0
Measured	44.3 ± 0.4	2.3 ± 0.1	36.0 ± 1.2	7.0 ± 0.2	7.0 ± 0.2	3.1 ± 0.3

Table 2. Glass properties.

Glass properties		
Density	ρ (g/cm ³)	2.774±0.001
Glass transition temperature	T_{g-DTA} (°C)	562±5
Dilatometric softening point	T_{s-Dil} (°C)	630±2
Thermal expansion coefficient	α_{300} (10 ⁻⁶ K ⁻¹)	11.16±0.14

3.2 Sintering and crystallization of glass powders

Figure 1 A and B illustrate the crystallization and sintering behavior of the glass powder size fractions (psf) under study, respectively. Figure 1 A summarizes DTA curves of the 12 psf under study (see Figure 11 and Table S1 in the supplementary material for characteristic temperatures). The glass transition temperature, T_g , appears at about 560 °C as a weak shoulder. The temperature range of sintering, T_s , is indicated by weak shoulders ranging between 650-700 °C for the psf <32 μm and 700-750 °C for the coarse psf 300-315 μm . After sintering, weak exothermic peaks or shoulders, T_{P-1} , could indicate a first crystalline phase. These effects are followed by a broad pronounced exothermic crystallization peak, T_{P-2} , shifting from 800 to 900 °C with increasing particle size. This broad peak shows additional weak shoulders indicating more than one crystalline phase. The crystallization of several phases is consistent with the occurrence of at least two endothermic melting dips, T_{M-1} and T_{M-2} , occurring above about 1150 °C and 1250 °C for all samples. Despite some scatter, these peaks do not depend on the glass particle size as expected for melting. Figure 1 A also shows a sharp distinct endothermal peak, T_F . In contrast to T_{M-1} and T_{M-2} , this peak slightly shifts from about 930 °C for psf <32 μm to about 980 °C for psf 300-315 μm . This finding indicates a diffusively controlled decomposition rather than melting. Consistently, the sample mass was found to decrease by 1-2.6 % until 1300 °C (not shown), and finer psf show a higher mass loss than coarser ones.

Figure 1 B illustrates the effect of particle size on sinterability. The onset temperature of sintering, T_{S0} (Figure 1 B), scatters at about 620 °C for all powders. The temperature of final shrinkage, T_{SE} , tends to increase with increasing particle size as expected. The finest particle size fraction <32 μm stands out with a very low value of T_{SE} , which may hint at the presence of a high fraction of fine particles. This fine powder compact area shrinks by about 38±3 % to about 95±1 % final relative density, FD , whereas the coarse powder compact densifies by only 25±2 % (300-315 μm). Detailed information is added in the supplementary material in Table S1.

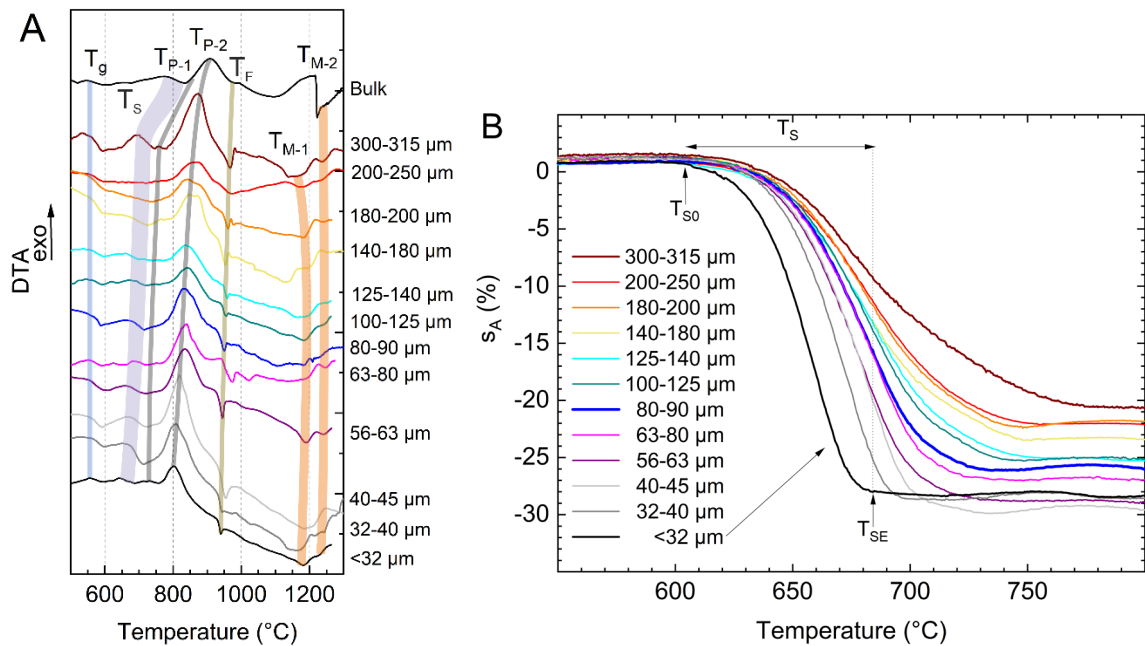


Figure 1. A: DTA curves of the glass powders under study and a bulk glass sample (≈ 2 mm). T_g : glass transition temperature, T_P : crystallization peak, T_M : melting peak temperature. B: Sintering of compacts pressed from the glass powders under study presented in terms of area shrinkage, s_A , calculated from the compact silhouette area during heating at 10 K/min versus temperature. T_{SO} sinter onset temperature, T_{SE} final densification temperature, and T_s sintering temperature range, shown for psf $<32\ \mu\text{m}$ in Figure 1 B (black curve).

3.3 Microstructure evolution

The microstructure evolution during sintering and subsequent crystallization is exemplarily illustrated in Figure 2, Figure 3, and Figure 4 for powder compacts of the psf 80-90 μm . Figure 2 compares shrinkage, densification, and the DTA curve for heating at 10 K/min. Figure 3 and Figure 4 depict micrographs heated at 10 K/min to different characteristic temperatures, quenched in air, and fractured. At the sintering onset (Figure 3 A, 630 $^{\circ}\text{C}$, $\rho_{rel} \approx 0.58$ %), fine and jagged particles stick on the surface of larger particles. These particles appear rounded after sintering to $\rho_{rel} \approx 0.62$ % at 652 $^{\circ}\text{C}$ (Figure 3 B), long before their larger counterparts do (Figure 3 C, 682 $^{\circ}\text{C}$, $\rho_{rel} \approx 0.75$ %). At this temperature, the first tiny crystallites appear at the particle surface (Figure 4 A), forming a thin surface layer at 693 $^{\circ}\text{C}$ (Figure 4 B). At 708 $^{\circ}\text{C}$ (Figure 3 D, Figure 4 C, $\rho_{rel} \approx 0.89$ %), these crystallites spread over the not-yet-sintered particle surface (arrow in Figure 3 D) and form an almost complete crystalline surface layer during late sintering at 728 $^{\circ}\text{C}$ ($\rho_{rel} \approx 0.92$ %, Figure 3 D, upper large pore). Sintering is then stopped at $\rho_{rel} \approx 0.93$ %, leaving a few irregularly shaped pores (Figure 3 E).

Despite this concomitant crystallization, Figure 3 E also reveals a weak net-like structure indicating thin layers of subsequent crystallites growing from the former fully sintered glass particle surface (arrows). After heating to 779 $^{\circ}\text{C}$ (Figure 3 F), these layers appear thicker and start to overgrow the entire glass bulk (Figure 3 G). As a result, new irregularly shaped small pores are formed (Figure 3 G, H), and the crystallite shape changes forming an irregularly feathery dendritic structure a (Figure 3 G, 862 $^{\circ}\text{C}$) to a more plate- or needle-like appearance (Figure 3 J, 1130 $^{\circ}\text{C}$).

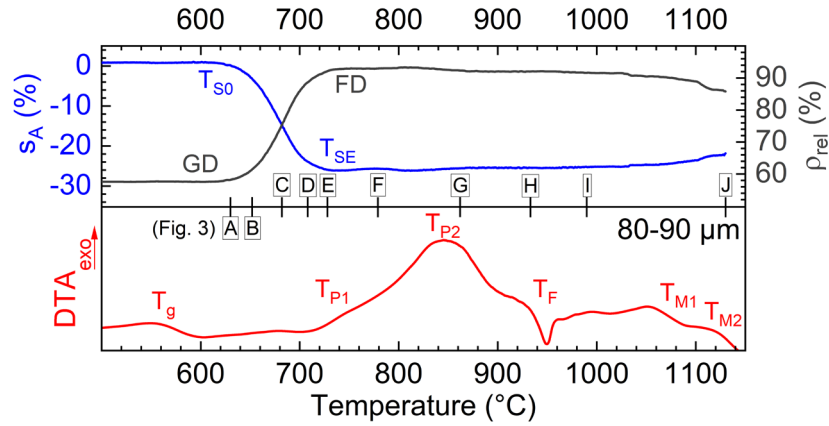


Figure 2. Combined area shrinkage, s_A , relative density, ρ_{rel} , calculated from the compact silhouette area and sample mass, and DTA curve for the particle size fraction 80-90 μm at 10 K/min. GD: initial relative compact density, FD: final compact density.

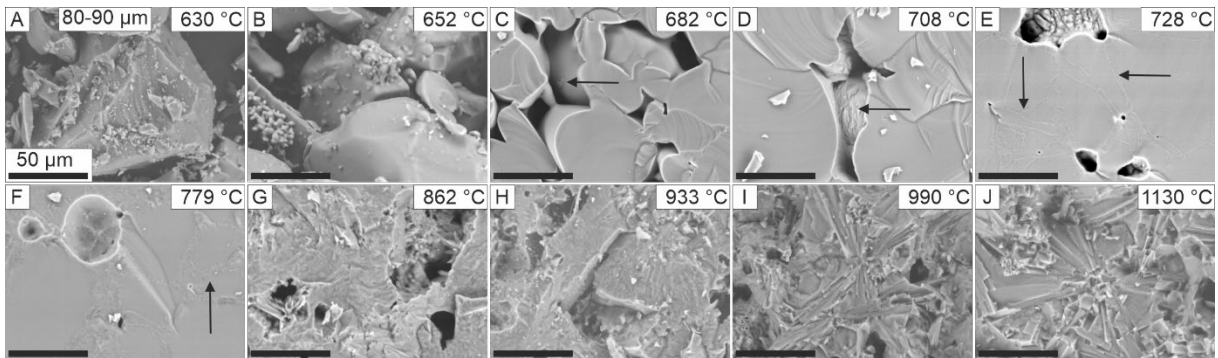


Figure 3. Micrographs of fracture surfaces of powder compacts of psf 80-90 μm after heating to different temperatures. Arrows mark growing surface crystallites.

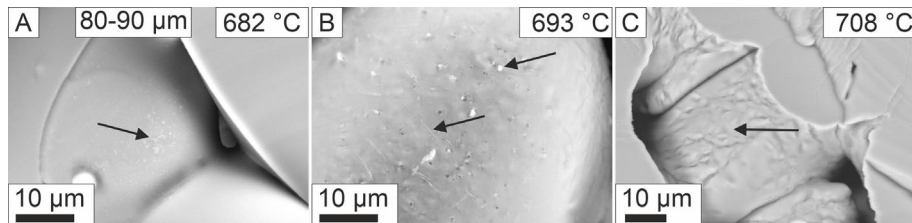


Figure 4. Micrographs of higher magnified fracture surfaces of powder compacts of psf 80-90 μm after heating to different temperatures. Arrows mark growing surface crystallites.

3.4 Crystal phases

Figure 5 shows XRD pattern measured on 80-90 μm compacts after heating to different temperatures. X-ray patterns of matching minerals taken from the “Crystallography Open Database” (COD) are shown in the bottom part of Figure 5. The temperature of densification is indicated by an arrow. Table 3 summarizes the identified phases.

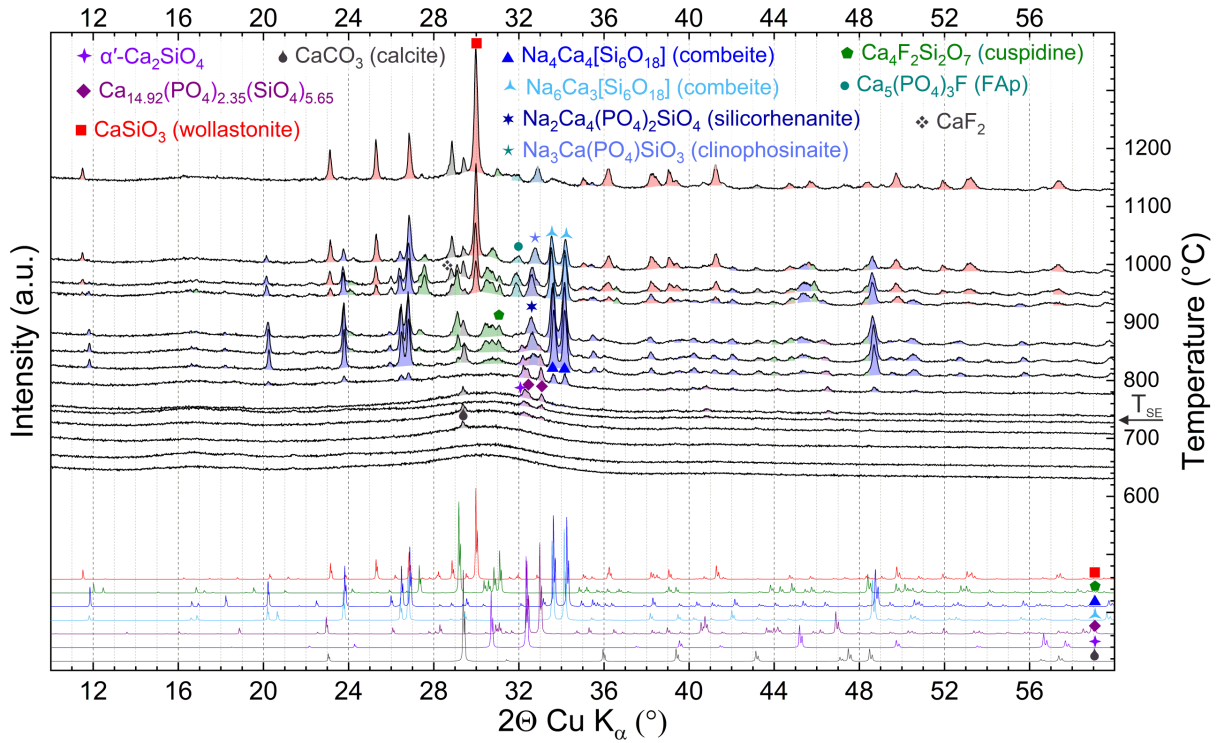


Figure 5. Upper part: XRD patterns of powder compacts (80-90 μm) heated to different temperatures at 10 K/min. These temperatures are shown by the curve intercepts with the right ordinate. Bottom: COD reference patterns measured on pure minerals. See Table 3 for crystal phases.

Table 3. Crystal phases detected in Figure 5. T_A : temperature of appearance, T_D : temperature of disappearance, n.d.: not detected ($> 1130\text{ }^\circ\text{C}$), PDF[®]: Powder Diffraction File. [#] $\text{Na}_6\text{Ca}_3[\text{Si}_6\text{O}_{18}]$ or, more precisely, $\text{Na}_{2.914}\text{Ca}_{1.543}\text{Si}_3\text{O}_9$ according to [25].

Name	Phase		T_A - T_D ($^\circ\text{C}$)	Symmetry	COD ID *PDF ID
Calcite	CaCO_3	◆	682	trigonal	9009669
Calcium orthosilicate	α' - Ca_2SiO_4	✦	682-862	hexagonal	1546028
Calcium phosphosilicate	$\text{Ca}_{14.92}(\text{PO}_4)_{2.35}(\text{SiO}_4)_{5.65}$	◆	682-862	orthorhombic	8103587
Combeite	$\text{Na}_4\text{Ca}_4[\text{Si}_6\text{O}_{18}]$	▲	693-960	trigonal	9007717
Combeite	$\text{Na}_6\text{Ca}_3[\text{Si}_6\text{O}_{18}]^{\#}$	▼	960-1130	trigonal	9007711
Cuspidine	$\text{Ca}_4\text{F}_2\text{Si}_2\text{O}_7$	◆	813-990	monoclinic	9014740
Calcium fluoride	CaF_2	◆	933-1130	cubic	9007064
Fluorapatite	$\text{Ca}_5(\text{PO}_4)_3\text{F}$	●	933- n.d.	hexagonal	9001879
Silicorhenanite	$\text{Na}_2\text{Ca}_4(\text{PO}_4)_2\text{SiO}_4$	★	813-949	hexagonal	32-1053*
Clinophosinaite	$\text{Na}_3\text{Ca}(\text{PO}_4)\text{SiO}_3$	★	949- n.d.	monoclinic	9011877
Wollastonite	CaSiO_3	■	933- n.d.	monoclinic	9005778

Below the temperature of densification, only a few weak XRD peaks indicate the presence of concomitant crystallization. In accordance with the micrograph Figure 4 A, where the first crystallites are visible at 682 $^\circ\text{C}$, the first XRD peaks slightly rise above the glassy halo at about 29.3 $^\circ$, 32.4 $^\circ$, and 33.0 $^\circ$. The peak at 29.3 $^\circ$ can be assigned to Calcite (CaCO_3 , ◆). The presence of calcite is most likely a result of glass corrosion during powder processing and storage [26], [19]. The calcite peak intensity does not correlate with the annealing temperature, and although previous studies [19] show that surface carbonates decompose already at 710 $^\circ\text{C}$, the CaCO_3 peak still occurs at 1130 $^\circ\text{C}$. This indicates a “secondary” corrosion of the annealed samples before the XRD measurement. This early decomposition below the densification of

most of the powders under study and the pronounced crystallization of F3 explains why sintering is not affected up to 800 °C (Figure 1 B) in the present case (see the discussion for more details).

The best match for the peaks at 32.4° and 33.0°, present up to just 862 °C, is orthorhombic calcium phosphosilicate ($\text{Ca}_{14.92}(\text{PO}_4)_{2.35}(\text{SiO}_4)_{5.65}$ (◆), referred to as CaPS hereafter) which shows peaks at about 33.0° and 32.4° [27]. α' - Ca_2SiO_4 also has its main peak at about 32.4° (✦). In this sense, the slight broadening of this peak could hint on the occurrence of this phase as well.

After further heating, the degree of crystallinity strongly increases. This temperature range is well above densification at 740 °C (Figure 1 B) and essential subsequent crystal growth into the interior of the glass powder particles is evident in Figure 3. At first, characteristic peaks of combeite are clearly present above 779 °C (▲). The two main reflections first appear at 33.6° and 34.3°, shift to 33.5° and 34.2° during further heating, reach their maximum intensity between 813 °C and 835 °C and decrease above 990 °C. The combeite modification $\text{Na}_4\text{Ca}_4[\text{Si}_6\text{O}_{18}]$ (▲) provides the best match below 960 °C, and $\text{Na}_6\text{Ca}_3[\text{Si}_6\text{O}_{18}]$ (▲) above.

Between 813 °C and 862 °C, the peaks at 32.4° and 33.0°, above assigned to CaPS, disappear. Instead, a new peak at 32.6° is detected, which corresponds with hexagonal silicorhenanite ($\text{Na}_2\text{Ca}_4(\text{PO}_4)_2\text{SiO}_4$, ★). This phase is not listed in COD but was available as a powder diffraction file (PDF). Above 949 °C this peak slightly shifts to 32.9° which leads to a better match with monoclinic clinophosinaite ($\text{Na}_3\text{Ca}(\text{PO}_4)\text{SiO}_3$, ★).

At 835 °C, further peaks between 30.3-31.0° become visible. These peaks match well with monoclinic cuspidine ($\text{Ca}_4\text{F}_2\text{Si}_2\text{O}_7$, ◆). At 933 °C, these peaks reach their maximum intensity and decrease afterwards. Two new weak peaks occur at 28.8° and 31.9° between 933 °C and 990 °C. The peaks at 28.8° and 31.8° can be assigned to cubic calcium fluoride (CaF_2 , ✧) and hexagonal $\text{Ca}_5(\text{PO}_4)_3\text{F}$ (fluorapatite, FAp, ●), respectively. However, due to the low peak intensities, a reliable classification is uncertain.

From 933 °C on, monoclinic wollastonite (CaSiO_3 , ■) is evident. The intensity of wollastonite-related peaks further increases while the intensity of all other present phases decreases. At 1130 °C, almost only wollastonite can be detected.

3.5 Crystallization of bulk glass samples

In order to better follow crystallization and its possible retardation effect on sintering, it was also studied on bulk glass samples. Figure 6 shows an annealed top surface used for surface nucleation density determination. The entire surface seems to be covered with irregularly shaped dendritic crystals, like in Figure 3. Some of them are labeled with dashed circles for better visualization. The surface nucleation density, N_s , was measured on annealed top surfaces and was found to be $665 \pm 62 \text{ mm}^{-2}$. This value corresponds to an average distance between neighboring crystals, d , of $38.5 \pm 2.8 \text{ }\mu\text{m}$.

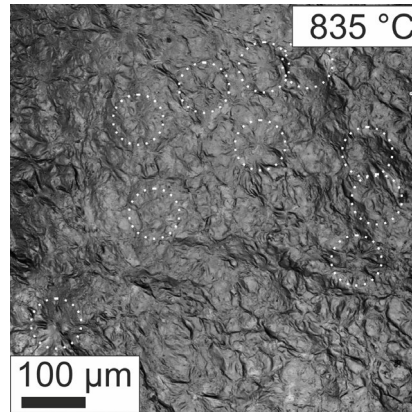


Figure 6. Top surface of bulk glass sample heated to 835 °C. Some crystalline structures are marked with dashed circles.

Figure 7 (A-L) shows cross sections of bulk samples heated at 10 K/min to different temperatures. Figure 7 (M-X) shows cross sections of bulk samples heated at 10 K/min to 838 °C and then subsequently held for different annealing times. For both treatments, Figure 7 reveals dendritic crystals forming an almost compact crystalline surface layer growing towards the bulk.

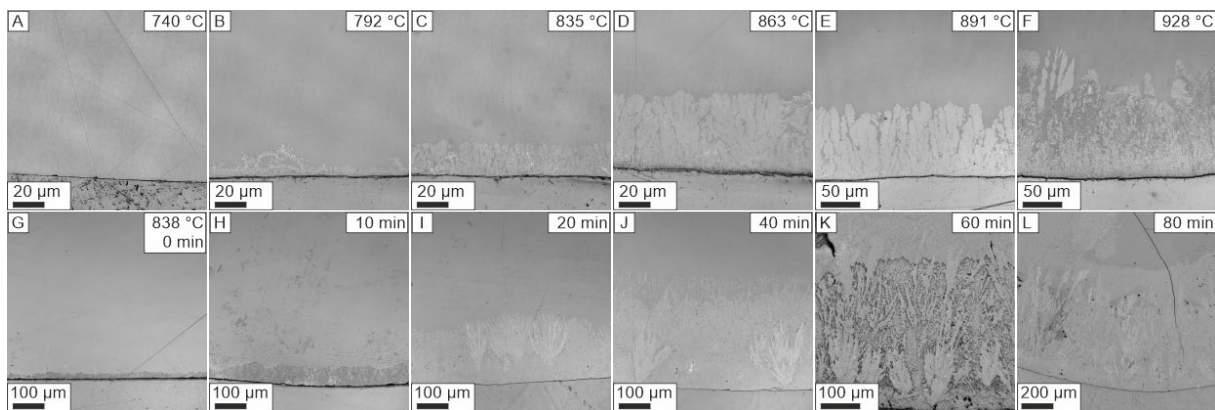


Figure 7. LSM micrographs of bulk samples of BG F3 heated at 10 K/min (A-F) and annealed at 838 °C (G-L).

The surface crystal diameter, D , and the crystalline layer thickness, L , were measured for both kinds of thermal treatments and are shown in Figure 8 A and B. In contrast to L , which progressively increases with the maximum temperature of heating, dD/dT decreases (Figure 8 A). This finding most likely reflects the impingement of surface crystallites, which did not allow measuring $D > 40 \mu\text{m}$. This impingement during heating at 10 K/min occurs at about 835 °C where $D = 33.1 \pm 9.4 \mu\text{m}$ and $L = 15.4 \pm 2.0 \mu\text{m}$. $D/L \approx 0.5$ hints on an almost isotropic crystal growth, where L corresponds to the crystal radius.

D and L measured at 838 °C are depicted in Figure 8 B. Again, D remains constant at $\approx 33 \pm 7 \mu\text{m}$ whereas L grows linearly. Its growth rate, U_L , could thus be simply estimated as $8.4 \pm 0.4 \mu\text{m}/\text{min}$. D and L measured during heating at 10 K/min are shown in Figure 8 A. U_L could be well fitted using the Arrhenius growth law [28]:

$$U_L(T) = U_0 \exp\left(\frac{-E_A}{R \cdot T}\right) \quad (1)$$

where U_0 is the pre-exponential factor, E_A the activation energy of crystal growth, and R the universal gas constant.

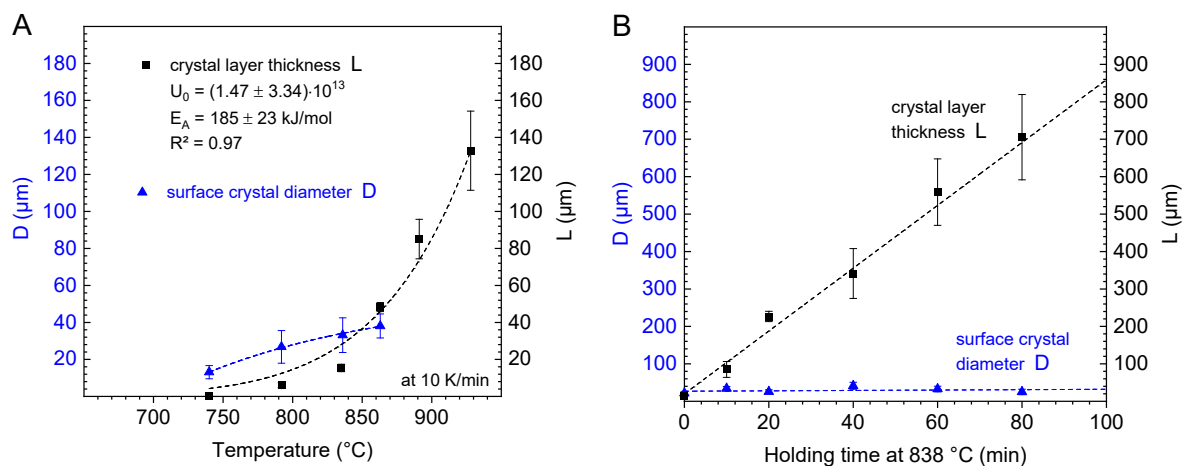


Figure 8. Surface crystal diameter D and crystalline layer thickness L measured on glass samples heated at 10 K/min to different temperatures (A) and annealed at 838 $^{\circ}\text{C}$ for different timescale (B), shown in Figure 7. The black dashed line in (A) is the Arrhenius fit with (1) and a linear fit in (B). The dashed blue lines are a guide for the eye.

Figure 9 shows EDX-maps of the crystalline surface layer growing inwards into a bulk glass sample annealed for 60 min at 838 $^{\circ}\text{C}$ as already depicted in Figure 7 K. The surface layer thickness is $L \approx 550$ μm as shown in Figure 7 B. A similar value would be reached during heating at 10 K/min only above 1000 $^{\circ}\text{C}$ (Figure 7), for which Figure 5 indicates the dominance of combeite and wollastonite. Confirming Figure 5 and Figure 7, Figure 9 thus indicates the simultaneous interlocked appearance of crystals of different chemical compositions. This effect might explain the linear growth of L with time observed in Figure 7 although the crystallization is not iso-chemical.

A closer look at Figure 9 indicates a triple-layer structure: a glassy area in the lower right corner (I), a primarily growing feathery middle part (II), and a more compact outermost crystalline layer (III). In layer I, the smooth and narrow grey value distribution in the BSE micrograph indicates amorphous material. Also, all major glass components are present.

Layer II is partly depleted in Na, whereas such overall depletion is not obvious for the other elements. However, their concentration appears more coarse-grained indicating the presence of chemically different small crystals, between which K is clearly enriched. According to Figure 5, these small dendrites could reflect the minor amount of orthorhombic calcium phosphosilicate seen in Figure 5 as the primary crystalline phase ($\text{Ca}_{14.92}(\text{PO}_4)_{2.35}(\text{SiO}_4)_{5.65}$, \blacklozenge). This phase is considered as a solid solution of calcium phosphate ($\text{Ca}_3(\text{PO}_4)_2$) in calcium orthosilicate ($\alpha\text{-Ca}_2\text{SiO}_4$, \blackstar) [27]. A calcium-phosphate crystal is possibly marked-up by the white oval in Figure 9. Most striking, however, layer II is penetrated by large-scaled dendrites enriched in Ca and F but depleted in K and Na whereas Si and P seem to be least affected. This finding is consistent with Figure 5, which reveals a pronounced amount of cuspidine ($\text{Ca}_4\text{F}_2\text{Si}_2\text{O}_7$, \blacklozenge) during later crystallization (above 813 $^{\circ}\text{C}$ during heating at 10 K/min).

In layer III, these large-scaled dendrites are still evident, although being separated by large crystals (or residual glass phase) enriched in Na and depleted in F, K, and Ca. The overall K depletion in this outermost, most fully crystallized layer indicated by Figure 9 K is reasonable since K is no inherent component of any of the detected crystalline phases.

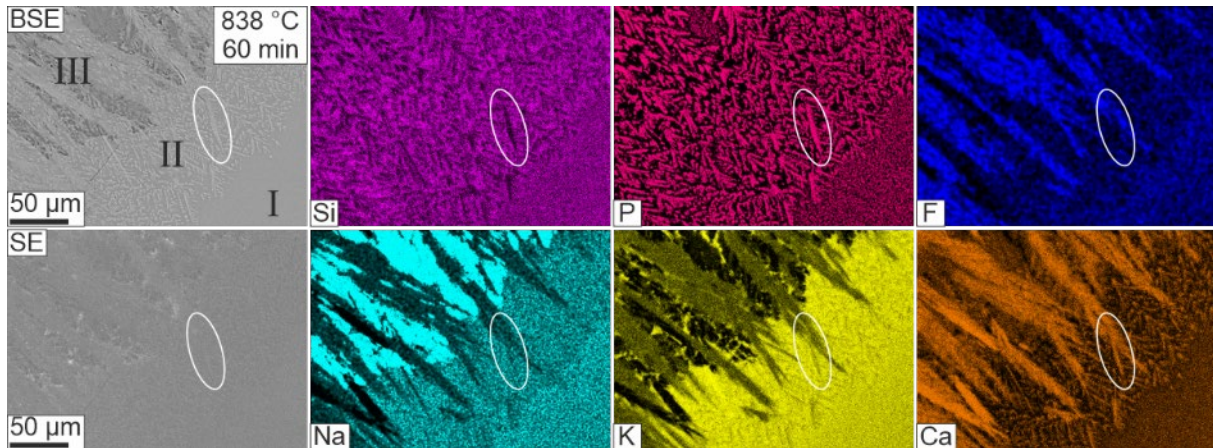


Figure 9. EDX-Mapping of a crystal surface layer growing inwards into a bulk glass sample annealed for 60 min at 838 °C (see also Figure 7 K). The white oval indicates a calcium phosphate crystallite.

4. Discussion

4.1 Crystallization

Figure 10 schematically illustrates the sequence of crystal phase evolution according to the peak assignments discussed above for the psf 80-90 µm. The amount of each crystal phase (neglecting CaCO₃ as a corrosion product) was estimated from their peak intensities shown in Figure 5. That of the amorphous phase was calculated from the intensity difference between the main crystal peak maximum and the amorphous halo beneath after removing the background. Crystallization becomes evident at ≈ 680 °C, where the first surface crystallites are visible in Figure 4 A. The maximum crystallinity is reached at 813 °C, above which wollastonite grows at the expense of all other crystal phases. Above this temperature, the ratio of the relative amount of all coexisting crystal phases and the amorphous background is about 11 %.

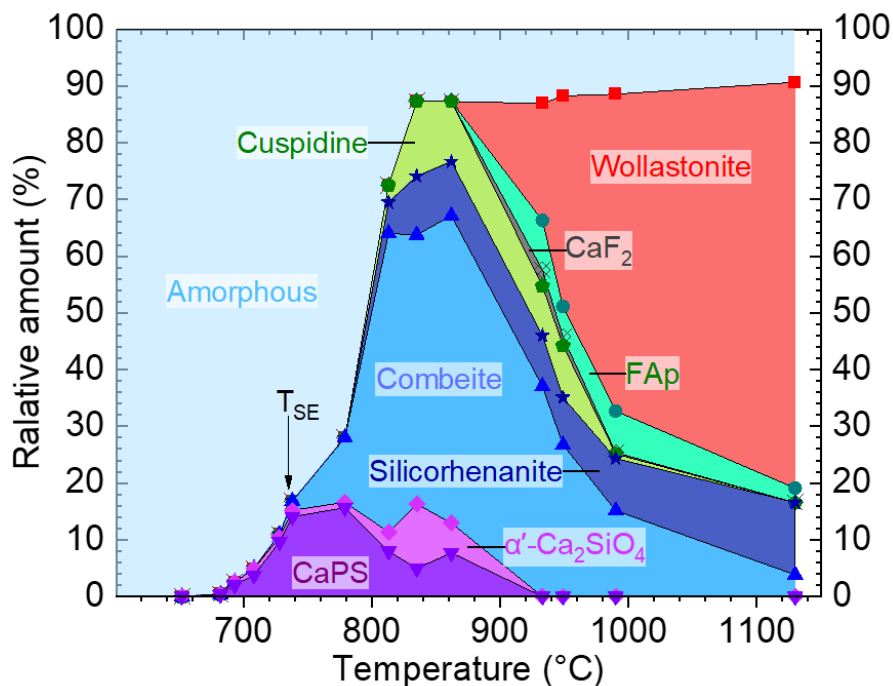


Figure 10. Normalized amounts of glass and crystal phases calculated from the peak intensities in Figure 5 for the psf 80-90 µm (neglecting CaCO₃).

4.1.1 Primary crystallization

The electron micrographs in Figure 4 and the X-ray diffraction pattern in Figure 5 for this psf reveal the first crystallites to occur after heating to 682 °C, where orthorhombic calcium phosphosilicate ($\text{Ca}_{14.92}(\text{PO}_4)_{2.35}(\text{SiO}_4)_{5.65}$), referred to as CaPS hereafter, was identified by XRD (◆). Phosphate-containing crystal phases have often been reported to occur as the primary crystal phase in bioactive glasses [29], [30]. Phosphate is supposed to exist as orthophosphate in the glass network before incorporation [31]. The above peak assignment was adapted from references [27] and [32], where CaPS is described as a solid solution and structure derivative of α' - Ca_2SiO_4 and the stoichiometry reflects the random distribution of phosphate in calcium orthosilicate forming a super lattice structure. Due to the limited content of phosphate in the glass melt (2.3 mol%, Table 1), however, the attainable fraction of CaPS is small.

Traces of α' - Ca_2SiO_4 was also detected by XRD (✦) in this early stage together with CaPS. A more pronounced amount, however, appears only above 813 °C, during the subsequent crystallization (Figure 10). Calcium orthosilicate has several polymorphs undergoing reversible phase transformations [33]. α - Ca_2SiO_4 is the high-temperature modification of the mineral. In the α' - Ca_2SiO_4 modification detected in Figure 5, however, the Si-tetrahedra are tilted from their position in α - Ca_2SiO_4 [32]. In this way, α' - Ca_2SiO_4 corresponds more closely to the monoclinic low-temperature modification β - Ca_2SiO_4 , which typically occurs between 630-680 °C [33]. The primary crystallization of an orthosilicate from the parent glass appears counterintuitive since the glass composition is close to that of calcium metasilicate (Table 1). Since only small amounts of α' - Ca_2SiO_4 was detected always together with other crystalline phases, its growth may occur in a chemically altered residual glass phase. Consistent with Figure 4 and Figure 5, the EDX mappings in Figure 9 reveals dendritic calcium phosphate with partially incorporated silicate as the primary crystal phase. The orthorhombic structure of CaPS corresponds to this growth characteristic, and a dendritic growth mechanism was found for Ca_2SiO_4 as well [34]. Although CaO and Si_2O are the most abundant oxides of the parent glass melt, the corresponding first weak exothermal shoulder in the DTA crystallization onset range (Figure 1) indicates that the amount of this phase is limited as well.

4.1.2 Subsequent crystallization

The majority of the DTA peak between 720 and 930 °C for the psf 80-90 μm in Figure 1, however, occurs above densification ($T_{SE} \approx 736$ °C) and represents the crystallization of combeite (▲, ▲). Combeite is a cubic close-packing arrangement of silicate tetrahedral [SiO_4] and octahedral alkali and alkaline-earth [M_4O_6] units and can be assigned to the group of cyclosilicates, consisting of elliptically distorted [Si_6O_{18}]-rings [35], [36]. It appears in two different modifications, $\text{Na}_4\text{Ca}_4[\text{Si}_6\text{O}_{18}]$ (▲) and $\text{Na}_6\text{Ca}_3[\text{Si}_6\text{O}_{18}]$ (▲). At elevated temperatures, an isomorphous solid-solution series is formed between the low-temperature modification of $\text{Na}_4\text{Ca}_4[\text{Si}_6\text{O}_{18}]$ and the high-temperature modification of $\text{Na}_6\text{Ca}_3[\text{Si}_6\text{O}_{18}]$. The replacement of Ca by two Na ions in the octahedral sites, leads to a change of the Si-O-Si bond angles uniformly 163° and results in less distorted, symmetric [Si_6O_{18}]-rings [35]. The transformation temperature between both modifications is proposed to be about 475 °C [35]. Thus, for $T > T_{SE} \approx 736$ °C, the high-temperature modification is therefore expected to appear. However, due to the low sodium content in the glass composition, the occupation of the octahedral sites by Na is limited. Thus, the peaks shown in Figure 5 up to 836 °C agree better with $\text{Na}_4\text{Ca}_4[\text{Si}_6\text{O}_{18}]$. Above 836 °C, however, $\text{Na}_6\text{Ca}_3[\text{Si}_6\text{O}_{18}]$ matches better. This seems to be the consequence of the consumption of calcium by the other crystallizing phases of wollastonite (CaSiO_3) and cuspidine ($\text{Ca}_4\text{F}_2\text{Si}_2\text{O}_7$) (Figure 5, Figure 10). The isothermal crystal growth rate, $U_L(t)$, of 8.4 ± 0.4 $\mu\text{m}/\text{min}$ at 838 °C, however, contains both the first growing dendritic CaPS and α' - Ca_2SiO_4 as well as the following combeite.

Above 850 °C, combeite starts to disappear. At 933 °C, the occurring peak at 32.6° in Figure 5 can be attributed to hexagonal silicorhenanite ($\text{Na}_2\text{Ca}_4(\text{PO}_4)_2\text{SiO}_4$, ★), whereas the peaks at 31.8° and 28.8° correspond with fluorapatite, FAp, ($\text{Ca}_5(\text{PO}_4)_3\text{F}$, ●) and CaF_2 (❖).

Thus, it can be assumed that cuspidine partially transforms in FAp and decomposes to CaF_2 . From studies of Bioglass® 45S5 it is also known that combeite transforms to silicorhenanite ($\text{Na}_2\text{Ca}_4(\text{PO}_4)_2\text{SiO}_4$) above 800 °C by incorporation phosphate into its structure [22], [37]. Silicorhenanite was found more previously for BG F3 psf <32 µm heated to 950 °C as well [15]. In addition, the amount of CaPS also decreases with the occurrence of silicorhenanite (Figure 10). This suggests that it also transforms into silicorhenanite. The shift of the silicorhenanite peak from 32.6° to 32.9° can be explained in the same way as the change of the combeite peaks. Due to the ongoing incorporation of calcium into wollastonite and combeite decomposition sodium is enriched. Thus, one calcium in the silicorhenanite structure is replaced by two sodium atoms which forms clinophosinaite (★) and distorts the hexagonal crystal structure to a monoclinic one.

Above 933 °C, wollastonite (CaSiO_3) starts to become the dominating crystal phase (Figure 5). Wollastonite is a pyroxenoid forming infinite chains of $[\text{SiO}_4]$ that share common vertices parallel to the b-axis [38]. Wollastonite matches the glass composition better than combeite and cuspidine can do together. Thus, up to 78.2 mol% wollastonite instead of 49 % or 18.6 %, could be formed from the BG F3, respectively (Table 1). This phase evolution is consistent with the ATR-FTIR spectra shown in Figure S2 included in the supplementary.

4.2 Carbonate and Fluoride

The peak at about 950 °C observed in Figure 1 A is endothermic and slightly decreases with decreasing particle size. It thus indicates a diffusion-controlled decomposition phenomenon rather than crystal melting. Decomposition phenomena are in fact indicated by the observed mass loss of 1-2.6 % up to 1300 °C. Two phenomena might be responsible for this peak: the decomposition of carbonate or the volatilization of fluoride.

Carbonate formation can result from the CO_2 uptake during powder processing and storage and its decomposition above densification can cause substantial gas bubble formation and foaming [26], [19], [39]. Due to the applied powder processing by jaw crushing and sieving, such uptake of CO_2 from the atmosphere cannot be excluded. However, the decomposition of surface carbonates should be almost complete at 710 °C [19]. For the range of particle size in this study, this should allow almost complete carbonate decomposition before densification. This way, no essential foaming was observed in the present case and the FTIR spectra in Figure S2, taken right after crushing and re-milling the heat-treated powder compacts (80-90 µm), do not show the typical carbonate double band in the range of 1300-1500 cm^{-1} .

On the other hand, calcite peaks are clearly present in Figure 5. Their appearance, however, seems to be rather random (see XRD curves for 725 °C and 780 °C, for instance, where no calcite is detected) and calcite is present even above 950 °C. The X-ray measurements were made after the IR spectroscopy, which enables further uptake of CO_2 and carbonate formation due to additional exposure of the re-milled specimens to air [26]. This finding once again underlines the high corrosion tendency of compositions with a high content of network modifiers such as bioactive glasses.

Therefore, carbonate decomposition could only contribute to a small extent to the observed endothermic peak. The minor influence of surface carbonates on sintering observed in the present study using crushed and sieved glass powders only, however, must not be generalized without care. Thus, pronounced foaming of fine (<32 µm) F3 and 13-93 powders milled in CO_2 atmosphere and in isopropanol was found in reference [19]. This foaming starts already at 700 °C for BG 13-93 and, crystallization retarded, at 950 °C for F3. Due to the perhaps more common milling in isopropanol, the findings in reference [19] might have more relevance for practical purposes.

Fluoride is known to volatilize from melts e.g. as HF or SiF_4 above 800 °C [3]. The Fluorine loss during melting strongly depends on several factors like the total fluorine content and the

network former/modifier ratio [3], [40], melting temperature and duration [41], [42]. For glasses in the system $\text{SiO}_2\text{-P}_2\text{O}_5\text{-CaO-CaF}_2$, the mass-loss of fluoride increases with higher phosphate content [43] and can reach 5-23 % [3], [5]. In the present case, XRF measurement, double-checked by pyrohydrolysis, reveals a low evaporation of fluoride during the glass melting process. Further, the main content of fluoride should be incorporated into cuspidine ($\text{Ca}_4\text{F}_2\text{Si}_2\text{O}_7$), which was found to partially decompose to wollastonite, CaF_2 , and FAp between 933 °C and 990 °C (Figure 5). CaF_2 decomposes itself and fluoride evaporates at this temperature [44], [40] (see Figure 10). The observed endothermic peak at about 950 °C is therefore most likely caused by the phase transformation of cuspidine to FAp and combeite to silicorhenanite. Such phase transformation could also be surface nucleated, which would explain its particle size dependence. The decomposition and evaporation of CaF_2 and calcite could only contribute to a minor extent at best.

With regard to a possible application in healthcare, both phases, carbonate, and CaF_2 , can be beneficial for the in vivo resorption and dissolution process. An increased amount of carbonate and fluoride can promote the formation of carbonated or fluorapatite. The first one can be formed faster, whereas fluorapatite has better mechanical properties than apatite [2], [8], [10].

4.3 Sinter retardation

All glass powders examined undergo substantial viscous flow sintering (Figure 1 B) yielding a pronounced densification between *GD* and *FD* of $\Delta\rho > 37\%$ (Table S1). Figure 1 B, however, also shows that the attainable shrinkage decreases with increasing particle size. The same trend is shown for $\Delta\rho$ in Table S1. For the fine psf < 63-80 μm , Figure 11 reveals that the temperature of densification, measured with heating microscopy, T_{SE} , is lower than the DTA onset temperature of the primary crystallization peak (Table S1). This means that sintering stops before crystallization is detectable with DTA. The microstructure evolution documented in Figure 3 and Figure 4 (80-90 μm) also shows a close coincidence of the first surface crystallites with the end of densification. This finding is consistent with the densification temperature $T_{SE} = 735\text{ °C}$ and the primary DTA onset temperature, $T_{O-1} = 721\text{ °C}$ measured for this psf (Table S1). All these findings indicate that sintering of BG F3 glass powders is retarded by surface crystallization.

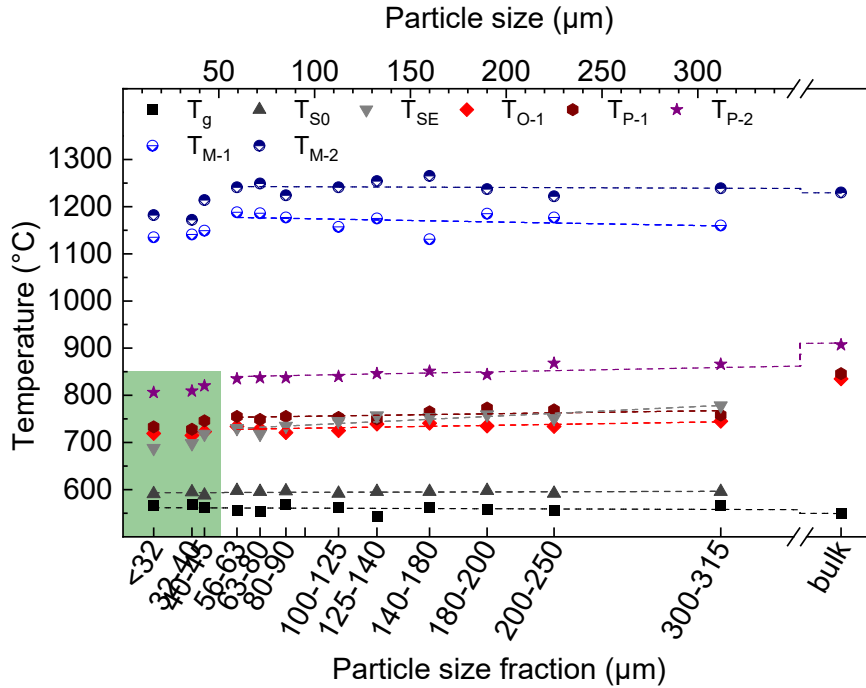


Figure 11. Characteristic sintering and crystallization temperatures for the glass powders under study heated at 10 K/min to different temperatures taken from Figure 1 A and B. T_g : glass transition, T_{SO} : sintering onset, T_{SE} : final densification, T_{O-1} , T_{P-1} , T_{P-2} : onset and peak of the first and second crystallization, T_{M-1} and T_{M-2} : maximum temperature of melting.

Surface crystallization related sinter retardation have been extensively studied in previous literature [45]. The most pronounced sinter retardation was found for isochemically crystallizing glasses with a strong surface nucleation tendency. In this case, surface crystals early impinge each other and form a thin compact crystalline surface layer. The kinetics of such sinter retardation phenomena could be well described as [46]:

$$s' = s'_0[1 - x_s] \quad (2)$$

where s' and s'_0 respectively represent the crystallization-retarded and the initial rate of viscous flow sintering and $[1-x_s]$ the non-crystallized *surface* fraction. Such a thin surface layer does not necessarily cause a detectable DTA effect [47]. A better correlation of sinter retardation with the DTA crystallization onset temperature, however, is expected for glasses with a less strong surface nucleation tendency. In this case, fewer crystals must grow to a larger size and volume fractions before crystal impingement occurs ($x_s \rightarrow 1$) and sintering fully stops. On the other hand, however, an enlarged effective viscosity of the partially crystallized glass melt must be considered [48] [49]. This, in turn, results in a progressively reduced viscous flow sintering rate, making it more likely that the onset of crystallization fully stops the not yet completed densification process.

In the present case, however, this situation could be even more complex due to the non-isochemical crystallization of F3. Figure 4 reveals first surface crystallites after heating to 682 °C showing plate- or needle-like shapes (Figure 4 B). Figure 5 and Table 3 indicate that these primary crystallites can be assigned to calcium orthosilicate (α' - Ca_2SiO_4 , \blacklozenge) and calcium phosphosilicate ($\text{Ca}_{14.92}(\text{PO}_4)_{2.35}(\text{SiO}_4)_{5.6}$, \blacklozenge). Figure 3 E indicates that these crystals cover a major part of the glass particle surface within the remaining pores after heating to 728 °C. This temperature correlates with final densification temperature of the psf 80-90 µm during analogous heating (Figure 1 B). The sinter retardation effect of this thin surface crystallization layer, however, is only moderate as Figure 1 B shows that sintering progressively proceeds beyond the final densification temperature, T_{SE} , found for the psf > 80-90 µm. This effect is not intuitive, as

an almost compact crystalline surface layer as indicated in Figure 3 E should strongly increase the effective surface viscosity.

This increase, however, could be partially mitigated by a crystallization induced decrease of glass viscosity due to potassium enriched in the residual glass phase between the dendrites (Figure 9), since none of the detected crystal phases contain K. The delay in sinter retardation with increasing particle size could also indicate that the surface nucleation density is not constant for all psf under study but decreases with decreasing particle size. Such phenomena can reflect the crystal nucleation activity of mechanical surface damage as well as the presence of nucleating milling abrasives [50].

These surface near phenomena, however, should be overlaid by the strong subsequent crystallization indicated in Figure 5 and Figure 10 at $T > 780$ °C above which, no further densification is evident in Figure 1 B for all psf under study. This pronounced crystallization effect is mainly related to the appearance of combeite. Assuming a constant and homogeneous glass composition according to Table 1, up to about 59 mol% Ca_2SiO_4 can be formed, which not seems enough to cover the particle surface for a sufficient retardation. Statistically seven SiO_4 -tetrahedra possess statistically about six calcium and two sodium atoms in their vicinity. Thus, for the formation of calcium orthosilicate (α' - Ca_2SiO_4 , \star) and combeite ($\text{Na}_4\text{Ca}_4[\text{Si}_6\text{O}_{18}]$, \blacktriangle) only two sodium atoms must migrate. The chemical composition of both phases together well resembles that of the glass (about 89 mol%). This can lead to a mutually enhancing crystallization rate as known from eutectic systems. In this sense, both crystal phases cause sinter retardation together after the appearance of $\text{Na}_4\text{Ca}_4[\text{Si}_6\text{O}_{18}]$. So, appearing crystallites can cover the entire glass particle easily, what can be seen in Figure 4 C, and explains the irregularly shaped surface layer seen in Figure 6 as well.

4.4 Rigid framework

After completed sintering, the pronounced crystallization of combeite is accompanied and the appearance of small amounts of cuspidine ($\text{Ca}_4\text{F}_2\text{Si}_2\text{O}_7$) (Figure 5). This establishes a crystalline network along the fully sintered former glass particle boundaries (Figure 3 E and F). As a result, the crystallization forms a three-dimensional rigid framework with encapsulated glassy regions which prevents softening of the sinter body.

Against the first impression, this special microstructure potential offers unexpected advantages. For targeted manufacturing of complex sinter bodies, e.g. by additive manufacturing, the softening of heated powder compacts is a danger for the shape stability and limits the design of microporosity and surface roughness. Both have a significant influence on potential cell ingrowth and attachment [51], [17]. The stiffening of the scaffold directly after the completed sintering by crystallization seems to have the potential for both the targeted design of surface roughness and the maintenance of microporosity.

Against this, the crystallized surface should reduce the degradation [52], [53], [54], [55], [56]. The effect of a surface layer with nanometers or a few micrometers thickness on bioactivity and degradation needs further investigation. Especially, after the discovery of nano-channels in bioactive glass-ceramics which even seem to accelerate apatite formation [57].

5. Conclusion

This study investigated the crystallization and sintering behavior of the fluoride containing bioactive glass F3. Bulk and powdered glass samples underwent entirely surface-induced crystallization and crystallites, which all essentially differ in their chemical composition from the glass melt. Due to its multi-component composition, crystallization involves several crystallization steps like the primary growth of α' - Ca_2SiO_4 and $\text{Ca}_{14.92}(\text{PO}_4)_{2.35}(\text{SiO}_4)_{5.65}$, the pronounced growth of combeite ($\text{Na}_2\text{Ca}_2\text{Si}_3\text{O}_9$) accompanied by the occurrence of cuspidine ($\text{Ca}_4\text{F}_2\text{Si}_2\text{O}_7$)

as well as the final growth of wollastonite (CaSiO_3), which becomes the dominating phase whereas combeite and cuspidine disappear and partially transform to silicorhenanite and fluorapatite at higher temperature. This complexity explains the observed linear growth of the multi-crystalline surface layer, but also the moderate retarding effect of crystallization on sintering. Due to the minor amount of primary crystal phase, dendritic crystal shapes and the expected presence of a K-enriched residual glass phase, surface crystallite impingement was not significant. Thus, relative final densities $FD \geq 91\%$ could be attained even for coarse glass powders whereas $FD \approx 95\%$ was attained for the finest powder under study ($<32\ \mu\text{m}$). However, the formation of a crystalline network along former sintered glass particles seems to be a powerful tool to stabilize the shape of a sintered body after densification.

Data availability statement

Data of presented results can be provided upon request.

Underlying and related material

Supplementary material is available at: <https://doi.org/10.5281/zenodo.15261386>

Author contributions

Carsten Blaeß: Conceptualization, Funding acquisition, Investigation, Methodology, Visualization, Writing – Original Draft.

Aldo R. Boccaccini: Conceptualization, Funding acquisition, Writing – Review & Editing

Ralf Müller: Conceptualization, Funding acquisition, Supervision, Writing – Original Draft

Competing interests

The authors have no conflict of interests to declare.

Funding

Financial support by the Deutsche Forschungsgemeinschaft DFG (grant numbers: MU 963/18-1, BO 1119/29-1, and BL 1936/1-1) is gratefully acknowledged.

Acknowledgement

We gratefully acknowledge experimental support by our colleague from BAM I. Feldmann for ESEM imaging and EDX measurement.

References

- [1] Brauer, D.S., *Bioactive Glasses—Structure and Properties*. Angewandte Chemie International Edition, 2015. 54(14): p. 4160-4181 DOI: <https://doi.org/10.1002/anie.201405310>.
- [2] Brauer, D.S., et al., *Fluoride-containing bioactive glasses: Effect of glass design and structure on degradation, pH and apatite formation in simulated body fluid*. Acta Biomaterialia, 2010. 6(8): p. 3275-3282 DOI: <https://doi.org/10.1016/j.actbio.2010.01.043>.
- [3] Brauer, D.S., M. Mneimne, and R.G. Hill, *Fluoride-containing bioactive glasses: Fluoride loss during melting and ion release in tris buffer solution*. Journal of Non-Crystalline

- Solids, 2011. 357(18): p. 3328-3333 DOI: <https://doi.org/10.1016/j.jnoncrysol.2011.05.031>.
- [4] Lusvardi, G., et al., *Fluoride-containing bioactive glasses: Surface reactivity in simulated body fluids solutions*. Acta Biomaterialia, 2009. 5(9): p. 3548-3562 DOI: <https://doi.org/10.1016/j.actbio.2009.06.009>.
- [5] Nommeots-Nomm, A., et al., *Phosphate/oxyfluorophosphate glass crystallization and its impact on dissolution and cytotoxicity*. Materials Science and Engineering: C, 2020. 117: p. 111269 DOI: <https://doi.org/10.1016/j.msec.2020.111269>.
- [6] Featherstone, J.D.B., *The science and practice of caries prevention*. Journal of the American Dental Association, 2000. 131(7): p. 887-899 DOI: <https://doi.org/10.14219/jada.archive.2000.0307>.
- [7] Mneimne, M., et al., *High phosphate content significantly increases apatite formation of fluoride-containing bioactive glasses*. Acta Biomaterialia, 2011. 7(4): p. 1827-1834 DOI: <https://doi.org/10.1016/j.actbio.2010.11.037>.
- [8] Gineste, L., et al., *Degradation of hydroxylapatite, fluorapatite, and fluorhydroxyapatite coatings of dental implants in dogs*. Journal of Biomedical Materials Research, 1999. 48(3): p. 224-234 DOI: [https://doi.org/10.1002/\(SICI\)1097-4636\(1999\)48:3<224::AID-JBM5>3.0.CO;2-A](https://doi.org/10.1002/(SICI)1097-4636(1999)48:3<224::AID-JBM5>3.0.CO;2-A).
- [9] Qu, H. and M. Wei, *Effect of fluorine content on mechanical properties of sintered fluoridated hydroxyapatite*. Materials Science and Engineering: C, 2006. 26(1): p. 46-53 DOI: <https://doi.org/10.1016/j.msec.2005.06.005>.
- [10] Lammers, P.C., et al., *Influence of Fluoride and Carbonate on Invitro Remineralization of Bovine Enamel*. Journal of Dental Research, 1991. 70(6): p. 970-974 DOI: <https://doi.org/10.1177/00220345910700061201>.
- [11] Moreno, E.C., M. Kresak, and Zahradni.Rt, *Fluoridated Hydroxyapatite Solubility and Caries Formation*. Nature, 1974. 247(5435): p. 64-65 DOI: <https://doi.org/10.1038/247064a0>.
- [12] Aaseth, J., et al., *Fluoride: A toxic or therapeutic agent in the treatment of osteoporosis?* The Journal of Trace Elements in Experimental Medicine, 2004. 17(2): p. 83-92 DOI: <https://doi.org/10.1002/jtra.10051>.
- [13] Vestergaard, P., et al., *Effects of treatment with fluoride on bone mineral density and fracture risk - a meta-analysis*. Osteoporosis International, 2008. 19(3): p. 257-268 DOI: <https://doi.org/10.1007/s00198-007-0437-6>.
- [14] Groh, D., F. Doehler, and D.S. Brauer, *Bioactive glasses with improved processing. Part 1. Thermal properties, ion release and apatite formation*. Acta Biomaterialia, 2014. 10(10): p. 4465-4473 DOI: <https://doi.org/10.1016/j.actbio.2014.05.019>.
- [15] Blaeß, C., et al., *Sintering and concomitant crystallization of bioactive glasses*. International Journal of Applied Glass Science, 2019. 10(4): p. 449-462 DOI: <https://doi.org/10.1111/ijag.13477>.
- [16] Hench, L.L., *The story of Bioglass (R)*. Journal of Materials Science-Materials in Medicine, 2006. 17(11): p. 967-978 DOI: <https://doi.org/10.1007/s10856-006-0432-z>.
- [17] Nawaz, Q., et al., *Processing and cytocompatibility of Cu-doped and undoped fluoride-containing bioactive glasses*. Open Ceramics, 2024. 18: p. 100586 DOI: <https://doi.org/10.1016/j.oceram.2024.100586>.
- [18] Doehler, F., et al., *Bioactive glasses with improved processing. Part 2. Viscosity and fibre drawing*. Journal of Non-Crystalline Solids, 2016. 432: p. 130-136 DOI: <https://doi.org/10.1016/j.jnoncrysol.2015.03.009>.
- [19] Blaeß, C. and R. Müller, *Sintering and foaming of bioactive glasses*. Journal of the American Ceramic Society, 2022. 105(11): p. 6616-6626 DOI: <https://doi.org/10.1111/jace.18626>.
- [20] Filho, O.P., G.P. La Torre, and L.L. Hench, *Effect of crystallization on apatite-layer formation of bioactive glass 45S5*. Journal of Biomedical Materials Research, 1996. 30(4): p. 509-514 DOI: [https://doi.org/10.1002/\(sici\)1097-4636\(199604\)30:4<509::aid-jbm9>3.0.co;2-t](https://doi.org/10.1002/(sici)1097-4636(199604)30:4<509::aid-jbm9>3.0.co;2-t).

- [21] Zandi Karimi, A., E. Rezabeigi, and R.A.L. Drew, *Crystallization behavior of combeite in 45S5 Bioglass® via controlled heat treatment*. Journal of Non-Crystalline Solids, 2018. 502: p. 176-183 DOI: <https://doi.org/10.1016/j.jnoncrysol.2018.09.003>.
- [22] Bretcanu, O., et al., *Sintering and crystallisation of 45S5 Bioglass® powder*. Journal of the European Ceramic Society, 2009. 29(16): p. 3299-3306 DOI: <https://doi.org/10.1016/j.jeurceramsoc.2009.06.035>.
- [23] Bose, S., et al., *Additive manufacturing of biomaterials*. Progress in Materials Science, 2018. 93: p. 45-111 DOI: <https://doi.org/10.1016/j.pmatsci.2017.08.003>.
- [24] Fernandes, H.R., et al., *Bioactive Glasses and Glass-Ceramics for Healthcare Applications in Bone Regeneration and Tissue Engineering*. Materials, 2018. 11(12): p. 2530 DOI: <https://doi.org/10.3390/ma11122530>.
- [25] Ohsato, H., I. Maki, and Y. Takeuchi, *Structure of Na₂CaSi₂O₆*. Acta Crystallographica Section C-Crystal Structure Communications, 1985. 41(Nov): p. 1575-1577 DOI: <https://doi.org/10.1107/S0108270185008617>.
- [26] Agea-Blanco, B., S. Reinsch, and R. Müller, *Sintering and Foaming of Barium Silicate Glass Powder Compacts*. Frontiers in Materials, 2016. 3: p. 10 DOI: <https://doi.org/10.3389/fmats.2016.00045>.
- [27] Saalfeld, H. and K.H. Klaska, *The Crystal-Structure of 6 Ca₂SiO₄ · 1 Ca₃(PO₄)₂*. Zeitschrift Fur Kristallographie, 1981. 155(1-2): p. 65-73 DOI: <https://doi.org/10.1524/zkri.1981.155.1-2.65>.
- [28] Arrhenius, S., *Über die Reaktionsgeschwindigkeit bei der Inversion von Rohrzucker durch Säuren*. Zeitschrift für Physikalische Chemie, 1889. 4U(1): p. 226-248 DOI: <https://doi.org/10.1515/zpch-1889-0416>.
- [29] Holand, M., et al., *Microstructure formation and surface properties of a rhenanite-type glass-ceramic containing 6.0 wt% P₂O₅*. Glass Science and Technology (Frankfurt), 2005. 78(4): p. 153-158.
- [30] Höland, W. and G.H. Beall, *Glass Ceramic Technology*. 2012, Westerville, OH, USA: John Wiley & Sons. 448 ISBN: 9780470487877.
- [31] Brauer, D.S., et al., *Structure of fluoride-containing bioactive glasses*. Journal of Materials Chemistry, 2009. 19(31): p. 5629-5636 DOI: <https://doi.org/10.1039/B900956F>.
- [32] Mumme, W.G., L.M.D. Cranswick, and B.C. Chakoumakos, *Rietveld crystal structure refinements from high temperature neutron powder diffraction data for the polymorphs of dicalcium silicate*. Neues Jahrbuch Fur Mineralogie-Abhandlungen, 1996. 170(2): p. 171-188.
- [33] Yamnova, N.A., et al., *Crystal structure of larnite β-Ca₂SiO₄ and specific features of polymorphic transitions in dicalcium orthosilicate*. Crystallography Reports, 2011. 56(2): p. 210-220 DOI: <https://doi.org/10.1134/S1063774511020209>.
- [34] Baek, J.-Y., et al., *Glass structure and crystallization via two distinct thermal histories: Melt crystallization and glass crystallization*. Journal of the European Ceramic Society, 2021. 41(1): p. 831-837 DOI: <https://doi.org/10.1016/j.jeurceramsoc.2020.08.036>.
- [35] Ohsato, H., Y. Takeuchi, and I. Maki, *Structure of Na₄Ca₄[Si₆O₁₈]*. Acta Crystallographica Section C, 1986. 42(8): p. 934-937 DOI: <https://doi.org/10.1107/S0108270186093940>.
- [36] Kahlenberg, V., *Concerning the incorporation of potassium in the crystal structure of combeite (Na₂Ca₂Si₃O₉)*. Mineralogy and Petrology, 2023. 117(2): p. 293-306 DOI: <https://doi.org/10.1007/s00710-022-00801-2>.
- [37] Coon, E., et al., *Viscosity and crystallization of bioactive glasses from 45S5 to 13-93*. International Journal of Applied Glass Science, 2021. 12(1): p. 65-77 DOI: <https://doi.org/10.1111/ijag.15837>.
- [38] Ohashi, Y., *Polysynthetically-Twinned Structures of Enstatite and Wollastonite*. Physics and Chemistry of Minerals, 1984. 10(5): p. 217-229 DOI: <https://doi.org/10.1007/Bf00309314>.
- [39] Müller, R., et al., *Foaming Species and Trapping Mechanisms in Barium Silicate Glass Sealants*. Advanced Engineering Materials, 2022. 24(6) DOI: <https://doi.org/10.1002/adem.202100445>.

- [40] Möncke, D., et al., *NaPO₃-AlF₃ glasses: Fluorine evaporation during melting and the resulting variations in structure and properties*. Journal of Chemical Technology and Metallurgy 2018. 53: p. 1047-1060.
- [41] Bueno, L.A., et al., *Study of fluorine losses in oxyfluoride glasses*. Journal of Non-Crystalline Solids, 2005. 351(52): p. 3804-3808 DOI: <https://doi.org/10.1016/j.jnoncrysol.2005.10.007>.
- [42] Szczodra, A., et al., *Fluorine losses in Er³⁺ oxyfluoride phosphate glasses and glass-ceramics*. Journal of Alloys and Compounds, 2019. 797: p. 797-803 DOI: <https://doi.org/10.1016/j.jallcom.2019.05.151>.
- [43] de Pablos-Martín, A., et al., *Fluorine loss determination in bioactive glasses by laser-induced breakdown spectroscopy (LIBS)*. International Journal of Applied Glass Science, 2021. 12(2): p. 213-221 DOI: <https://doi.org/10.1111/ijag.15867>.
- [44] Qi, Q., et al., *[Stability of CaF₂ at high temperature]*. Huan Jing Ke Xue, 2002. 23(3): p. 111-4.
- [45] Müller, R. and S. Reinsch, Viscous phase silicate processing, in Ceramics and composites processing methods, N. Bansal and A.R. Boccaccini, Editors. 2012, John Wiley Sons Inc.: Hoboken, NJ. p. 75-144 ISBN: 978-0-470-55344-2.
- [46] Müller, R., On the kinetics of sintering and crystallization of glass powders. Glastechnische Berichte-Glass Science and Technology, 1994. 67C: p. 93-98.
- [47] Muller, R., The Influence of Grain-Size on the Overall Kinetics of Surface-Induced Glass Crystallization. Journal of Thermal Analysis and Calorimetry, 1989. 35(3): p. 823-835 DOI: <https://doi.org/10.1007/Bf02057238>.
- [48] Gutzow, I., et al., The kinetics of surface induced sinter crystallization and the formation of glass-ceramic materials. Journal of Materials Science, 1998. 33(21): p. 5265-5273 DOI: <https://doi.org/10.1023/A:1004400508154>.
- [49] Karamanov, A. and M. Pelino, Sinter-crystallization in the diopside-albite system part II. Kinetics of crystallization and sintering. Journal of the European Ceramic Society, 2006. 26(13): p. 2519-2526 DOI: <https://doi.org/10.1016/j.jeurceramsoc.2005.12.007>.
- [50] Muller, R., E.D. Zanotto, and V.M. Fokin, *Surface crystallization of silicate glasses: nucleation sites and kinetics*. Journal of Non-Crystalline Solids, 2000. 274(1-3): p. 208-231 DOI: [https://doi.org/10.1016/S0022-3093\(00\)00214-3](https://doi.org/10.1016/S0022-3093(00)00214-3).
- [51] Liu, X., M.N. Rahaman, and Q. Fu, *Bone regeneration in strong porous bioactive glass (13-93) scaffolds with an oriented microstructure implanted in rat calvarial defects*. Acta Biomaterialia, 2013. 9(1): p. 4889-4898 DOI: <https://doi.org/10.1016/j.actbio.2012.08.029>.
- [52] Wang, Q.B., Q.G. Wang, and C.X. Wan, *Effect of sintering time on the microstructure and properties of inorganic polyphosphate bioceramics*. Science of Sintering, 2010. 42(3): p. 337-343 DOI: <https://doi.org/10.2298/sos1003337w>.
- [53] Schaefer, S., et al., *How Degradation of Calcium Phosphate Bone Substitute Materials is influenced by Phase Composition and Porosity*. Advanced Engineering Materials, 2011. 13(4): p. 342-350 DOI: <https://doi.org/10.1002/adem.201000267>.
- [54] Jones, J.R., *Review of bioactive glass: From Hench to hybrids*. Acta Biomaterialia, 2013. 9(1): p. 4457-4486 DOI: <https://doi.org/10.1016/j.actbio.2012.08.023>.
- [55] Plewinski, M., et al., *The effect of crystallization of bioactive bioglass 45S5 on apatite formation and degradation*. Dental Materials, 2013. 29(12): p. 1256-1264 DOI: <https://doi.org/10.1016/j.dental.2013.09.016>.
- [56] Boccaccini, A.R., et al., *Sintering, crystallisation and biodegradation behaviour of Bioglass®-derived glass-ceramics*. Faraday Discussions, 2007. 136: p. 27-44 DOI: <https://doi.org/10.1039/b616539g>.
- [57] Kirste, G., et al., *Bioactive glass-ceramics containing fluorapatite, xonotlite, cuspidine and wollastonite form apatite faster than their corresponding glasses*. Scientific Reports, 2024. 14(1): p. 3997 DOI: <https://doi.org/10.1038/s41598-024-54228-0>.